2D Flow Field Analysis by the Exergetic Method

Miguel Angel Aguirre, Sébastien Duplaa, Xavier Carbonneau

2D Flow Field Analysis by the Exergetic Method

Miguel A. Aguirre[1] Sébastien Duplaa[2] and Xavier Carbonneau[3]
ISAE-SUPAERO, Toulouse University, 31055, France

This paper performs an analysis of the flow field around an airfoil by using the exergetic method. It offers a new way to analyze the aerodynamics based on an energetic reasoning rather than a classical mechanical point of view (represented by the far-field method). The objective is to explore the usage of this method as a tool for the aerodynamic assessment of a classical airfoil: the exergetic parameters are related with physical phenomena, and specifically used to detect the origin of losses. CFD analyses of a NACA 0012 airfoil at subsonic and transonic conditions were used as test cases to present the concept.

Nomenclature

$\dot{\mathcal{A}}$	=	total anergy outflow rate, W
$\dot{\mathcal{A}}_{\Phi}$	=	viscous anergy rate created inside the control volume, W
$\dot{\mathcal{A}}_{\nabla T}$	=	thermal anergy rate, W
$\dot{\mathcal{A}}_{w}$	=	shockwave anergy rate, W
a	=	speed of sound, $m.s^{-1}$
α	=	angle of attack, Degrees
C_D	=	drag coefficient
c	=	airfoil chord, m
c_p	=	mass specific heat at constant pressure, $J.kg^{-1}.K^{-1}$
D	=	drag force, N
$\delta(\,)$	=	$(\,) - (\,)_0$, local variation of a parameter respect to the upstream value
$\dot{E}_u$	=	axial kinetic exergy outflow rate, W

[1] Research and development engineer, DAEP-Department of Aerodynamics, Energetics and Propulsion.
[2] Associate professor, DAEP-Department of Aerodynamics, Energetics and Propulsion.
[3] Associate professor, DAEP-Department of Aerodynamics, Energetics and Propulsion.

$\dot{E}_v$ = transverse kinetic exergy outflow rate, W

$\dot{E}_p$ = boundary-pressure work rate, W

e = mass specific internal energy, J.kg^{-1}

$\dot{\varepsilon}_m$ = mechanical exergy outflow rate across the survey plane, W

$\dot{\varepsilon}_{th}$ = thermal exergy outflow rate, W

Φ_{eff} = effective dissipation, J.s^{-1}.m^{-3}

γ = ratio of specific heats

h_t = mass specific total enthalpy, J.kg^{-1}

$\boldsymbol{i, j, k}$ = unit vectors along the aerodynamic x-, y- and z-axes

k_{eff} = Fourier law's coefficient

M = Mach number (= u_0/a_0)

μ, μ_t = laminar and turbulent dynamic viscosities, kg.m.s^{-1}

P_s, P_t = static and total pressure, Pa

Pr = Prandtl number (= $c_p \mu / k$)

Re = Reynolds number (= $\rho_0 \, u_0 \, c / \mu_0$)

ρ = air density, kg.m^{-3}

S = surface, m^2

s = mass specific entropy, J.kg^{-1}.K^{-1}

T_s, T_t = static and total temperatures, K

$\boldsymbol{V}$ = u**i**, v**j**, w**k**, local velocity vector, m.s^{-1}

Subscripts

0 = Upstream values

ref = reference

b = body

wave = shockwave enclosing surface or volume

I. Introduction

THE flow field analysis is one of the most important aspects of the aerodynamic assessment of a given aircraft configuration. The classical approach is based on the field visualization of several aero-thermodynamic parameters like velocity, pressure, temperature, and so on. More recently, the far-field drag prediction methods enabled the visualization of the drag components (viscous, vortex and wave) in the wake of a body [1]. However, new aerodynamic tools have been developed recently, of which the most promising methods are the Power Balance [2] and the exergy analysis [3]. These two approaches have been extensively used for the quantitative performance assessment of future aircraft configurations like boundary layer ingestion designs [4]. One of the major assets of these methods is their powerful insight into the physics. As a matter of fact, the bodies are studied following a very intuitive mechanical/energetic approach.

In spite of the inherent advantages offered by these methods, they are not currently used to perform the qualitative analysis of flow fields on external aerodynamics applications (it was only used very recently for internal aerodynamics applications [5]). As a consequence, this work explores this possibility, highlighting its usefulness and potentials.

Given that the exergy method is considered as a generalization of the Power balance, only the Exergy Method will be discussed here, but the results are also valid for the Power Balance method.

II. Review of the aerodynamic assessment methods

A. System of reference

The reference system used hereafter is shown in Fig. 1.

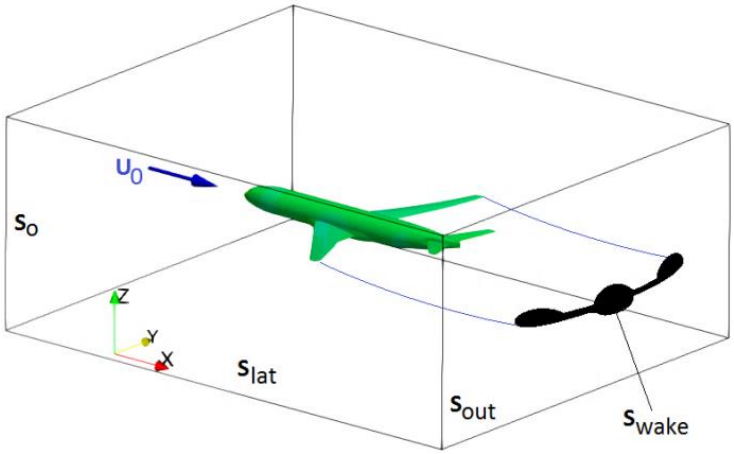

Fig. 1 Conventional reference frame.

It has the x-axis aligned with the upstream flow direction and pointing rearwards, the y-axis points towards the right-hand side of the body and the z-axis points upwards. Moreover, when control volume formulations are used, it is assumed that the outlet section "S_{out}" of the control volume is a plane (called "survey plane") and it is placed normal to the x-axis. Also, the lateral surfaces are considered parallel to the upstream direction and far away from the body.

B. Far-field method

The far-field methods apply the momentum conservation equation to a control volume surrounding the body in order to define a set of equations thereby allowing a phenomenological decomposition of drag while, giving at the same time, a good insight into the physics. Several variants of this method are available [6-9], each that allow the extraction of the drag force by only analyzing the wake of a body, but here we will discuss only the most recent approach for the wind tunnel measurement of stationary flows [1]. It is based on the small perturbations method and the decomposition of the axial velocity deficit inside the wake. This leads to the following profile drag equation which is valid for compressible and incompressible regimes:

$$D_{profile} = \frac{\rho_0 {u_0}^2}{2} \int_{S_{wake}} \left[-\frac{2}{\gamma {M_0}^2} \Delta P_t - \Delta T_t + \left(1 - \frac{{M_0}^2}{4}\right) {\Delta T_t}^2 - \Delta P_t \, \Delta T_t - \left(1 - {M_0}^2\right)\left(\Delta \bar{u}^2 + 2 \, \Delta u^* \, \Delta \bar{u}\right) \right] dS \quad (1)$$

Where:

$$\Delta Pt = \frac{P_t}{P_{t_0}} - 1 \quad (2)$$

$$\Delta Tt = \frac{T_t}{T_{t_0}} - 1 \quad (3)$$

$$\Delta u = \frac{u}{U_0} - 1 \quad (4)$$

$$\Delta u^* = \sqrt{1 - \frac{2}{(\gamma - 1)\,{M_0}^2}\left(\left(\frac{P_s}{P_{s_0}}\right)^{\frac{(\gamma-1)}{\gamma}} - 1\right) - \frac{v^2 + w^2}{{U_0}^2}} - 1 \quad (5)$$

$$\Delta \bar{u} = \Delta u - \Delta u^* \quad (6)$$

The "small perturbation" assumption considers that the variations of total pressure ΔP_t, total temperature ΔT_t and velocity Δu are small. Moreover, the velocity perturbation Δu is decomposed into a viscous contribution $\Delta \bar{u}$ (which is null outside the wake) and other component Δu^* that is related to the isentropic field.

For 2D applications, the profile drag is the total drag acting upon a body (which includes the viscous drag and the wave drag). The drag forces will be nondimensionalized following the classical approach, and its drag coefficient value presented in drag counts, defined as one ten thousandth of Cd (1dc = 0.0001 Cd).

C. Exergy method

The exergy approach is based on the 1st and 2nd laws of thermodynamics [10, 11]. It decomposes the total energy of a system into two components: the exergy "ε" (the useful part of the energy) and the anergy "$\mathcal{A}$" (its useless part). The exergy concept states that any perturbation of the system (perturbation of speed, pressure, and so on) has an inherent energetic potential and can be returned to its original (equilibrium) state and converted into work by means of a reversible transformation. This can be expressed as follows:

$$\varepsilon = \delta h_t - T_{s_0}\,\delta S = \delta h_t - \mathcal{A} \tag{7}$$

Several authors have used this concept in order to evaluate the external aerodynamic behavior of flight vehicles [12-15]. One of most recent formulations is the one proposed by Arntz [3]: an exergy approach well suited for the analysis of CFD simulations and valid for compressible and incompressible flows. This exergetic formulation obtains the so-called "exergetic drag coefficient" when an unpowered and adiabatic case is considered. It is given by the following expression, which performs an exergetic-based breakdown of the drag coefficient [16]:

$$C_{D_\varepsilon} = \frac{\dot{\varepsilon}_m + \dot{\varepsilon}_{th} + \dot{\mathcal{A}}_\Phi + \dot{\mathcal{A}}_{\nabla T} + \dot{\mathcal{A}}_w}{\frac{1}{2}\rho_0\, u_0{}^3\, S_{ref}} \tag{8}$$

Each term represents an equation itself as indicated as follows:

$$\dot{\varepsilon}_m = \underbrace{\int_{Sout} \tfrac{1}{2}\rho\,\delta u^2 (\vec{V}.\vec{n}) dS}_{\dot{E}_u} + \underbrace{\int_{Sout} \tfrac{1}{2}\rho(v^2+w^2)(\vec{V}.\vec{n}) dS}_{\dot{E}_v} + \underbrace{\int_{Sout} (P_s - P_{s_0})[(\vec{V}-\vec{V}_0).\vec{n}] dS}_{\dot{E}_p} \tag{9}$$

$$\dot{\varepsilon}_{th} = \int_{Sout} \rho\,\delta e\,(\vec{V}.\vec{n})\,dS + \int_{Sout} P_{s_0}(\vec{V}.\vec{n})\,dS - \underbrace{T_{s_0}\int_{Sout} \rho\,\delta s\,(\vec{V}.\vec{n})}_{\dot{\mathcal{A}}}\,dS \tag{10}$$

$$\dot{\mathcal{A}}_\Phi = \int_v \frac{T_{s_0}}{T_s}\,\Phi_{eff}\,dv \tag{11}$$

$$\dot{\mathcal{A}}_{\nabla T} = \int_v \frac{T_{s_0}}{T_s{}^2}\,k_{eff}\,(\nabla T)^2\,dv \tag{12}$$

$$\dot{\mathcal{A}}_w = T_{s_0}\int_{S_{wave}} (\rho\,\delta s\,\vec{V}).\vec{n}\;\; dS \;=\; \int_{SW_{vol}} \nabla.(T_{s_0}\,\rho\,\delta s\,\vec{V})\;\; dsw_{vol} \tag{13}$$

$$\kappa_{eff} = c_p\left(\left(\frac{\mu}{Pr}\right) + \left(\frac{\mu_t}{Pr_t}\right)\right) \quad (14)$$

$$\Phi_{eff} = (\overline{\overline{\tau}}.\nabla).\vec{V} \quad (15)$$

The mechanical exergy outflow rate $\dot{\varepsilon}_m$ represents the amount of mechanical power that can be recovered by a so-called exergy recovery system (e.g., BLI). It is related to the axial and transverse velocity perturbations ($\dot{E}_u$ and $\dot{E}_v$ respectively) and the pressure perturbations $\dot{E}_p$. The thermal exergy outflow rate $\dot{\varepsilon}_{th}$ represents the amount of thermal power that can be recovered. If the exergies are not valued (recovered) they will be gradually destroyed downstream, becoming a loss. On the other hand, the total anergy $\dot{\mathcal{A}}$ represents the total amount of energy that has been already lost by the system (quantified by the entropy increase). It can be decomposed into the viscous losses $\dot{\mathcal{A}}_{\Phi}$, the thermal losses $\dot{\mathcal{A}}_{\nabla T}$ and the shockwave losses $\dot{\mathcal{A}}_w$ (if any). Please note that not only does viscous and thermal anergy creation take place inside the boundary layer but also inside the wake.

Hereafter, the exergy-based drag coefficient will be displayed in "power counts" (pc), defined as one tenth thousandth of "Cd_ε" (1pc = 0.0001 Cd_ε). Indeed, the exergy-based drag coefficient is equivalent to the force-based drag coefficient, thus, the power counts and drag counts units will be used interchangeably throughout this paper.

III. CFD data

The exergy-based flow field analysis performed in this article is based on 2D CFD data. The case study is a NACA 0012 airfoil with a sharp trailing edge. A C-block structured grid with wake refinement was used with a domain extent of 150 chords in all directions. The mesh blocking and refinement in the wake region was different for each angle of attack: the refinement zone follows the wake deviation in order to ensure a proper capture of the wake. A grid convergence study was performed and the near-field drag value compared against experimental data of the bibliography [17-19] as shown in Fig.2. Then the mesh of 593,000 cells was selected, which ensured the correct capture of all the physical phenomena even in transonic conditions.

RANS simulations were performed with the Spalart Allmaras turbulence model for several angles of attack and several Mach numbers, with a fixed Reynolds number of $3x10^6$. For each case, a first quick convergence was made with a first-order discretization (flow and turbulence) to about 3000 iterations, followed by a final second-order discretization convergence as shown in Fig. 3. The simulations were left running until the near-field drag coefficient residual was less than 0.1 drag counts. At the same time, the residuals must reach their maximum precision in order

to ensure that the airfoil's losses were completely transmitted (convected) downstream. Then, the y^+ parameter was controlled in order to verify that $y^+ \leq 1$ everywhere around the body (as required by the Spalart Allmaras model). The resulting CFD data was analyzed with a Paraview plugin called Epsilon, previously developed at ISAE-SUPAERO, which performs a far-field and exergetic analysis.

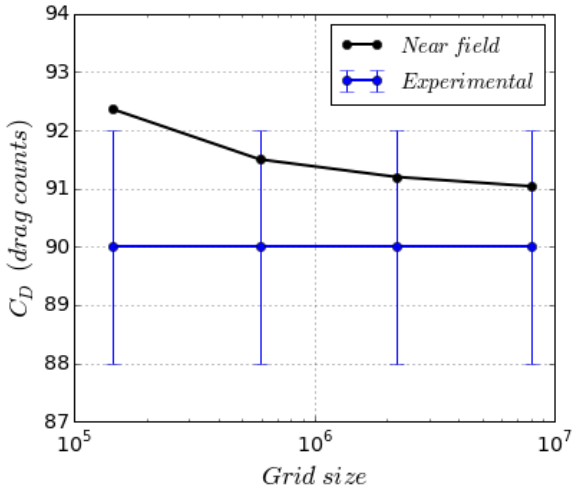

Fig. 2 Grid convergence for α=0°, M=0.3 and Re=3x10^6

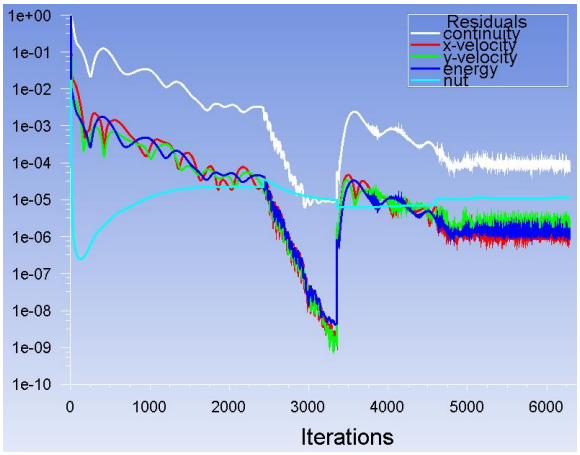

Fig. 3 Residual convergence for the airfoil at α=0°/M=0.3

IV. Exergetic-based flow field analysis of an airfoil

A. M=0.3 / α=0°

The simplest case to start with is the classic airfoil at low speed with zero angle of attack. We will study first its exergy components and then the anergy components.

In order to understand the axial kinetic exergy field, a systematic approach is presented in Figs. 4, 5 and 6. First, the axial velocity field is shown in Fig.4, where the typical flow phenomena are observed: a stagnation point at the leading edge, a curvature-based acceleration region around the airfoil and the low-speed region inside the boundary layer and viscous wake. Moreover, a black survey line is placed downstream of the airfoil, along which is plotted the axial velocity profile, putting in evidence the velocity deficit inside the wake. The second step is to analyze the axial velocity perturbation field shown in Fig.5. Note that the perturbation is negative at the stagnation and wake regions, but positive in the high-speed regions at the maximum thickness position of the airfoil. The survey line again allows observing the velocity deficit inside the wake, which is used by the far-field methods in order to extract the far-field drag. Finally, the axial kinetic exergy field shown in Fig. 6 can be analyzed, where the integrand of the axial kinetic exergy equation "E_u" is plotted at each point of the domain and along the survey line.

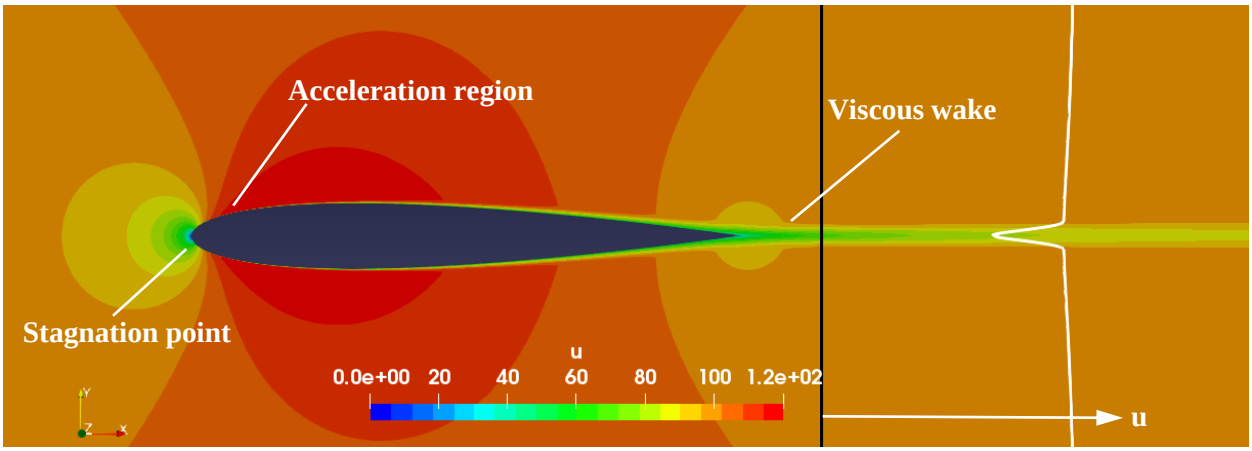

Fig. 4 Axial velocity field [m/s]

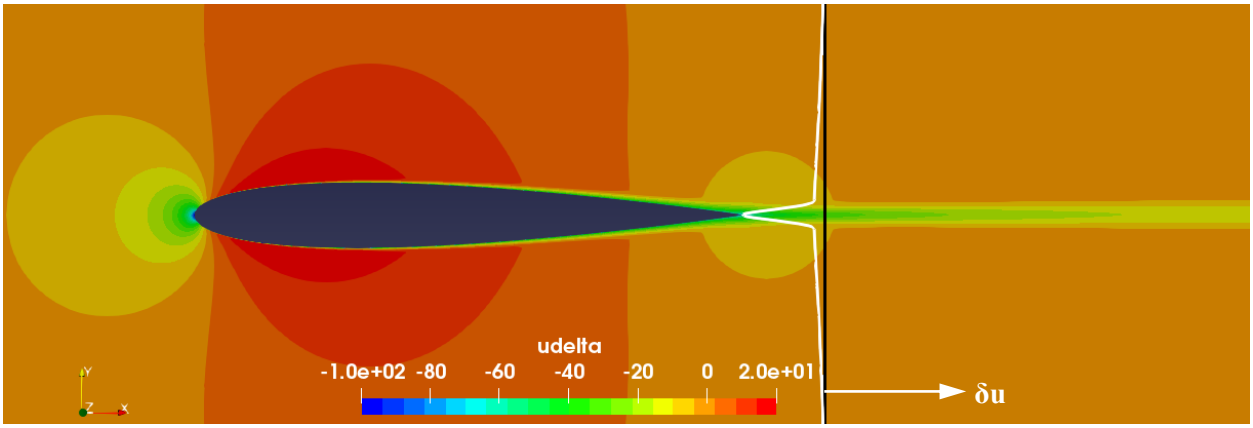

Fig. 5 Axial velocity perturbation field [m/s]

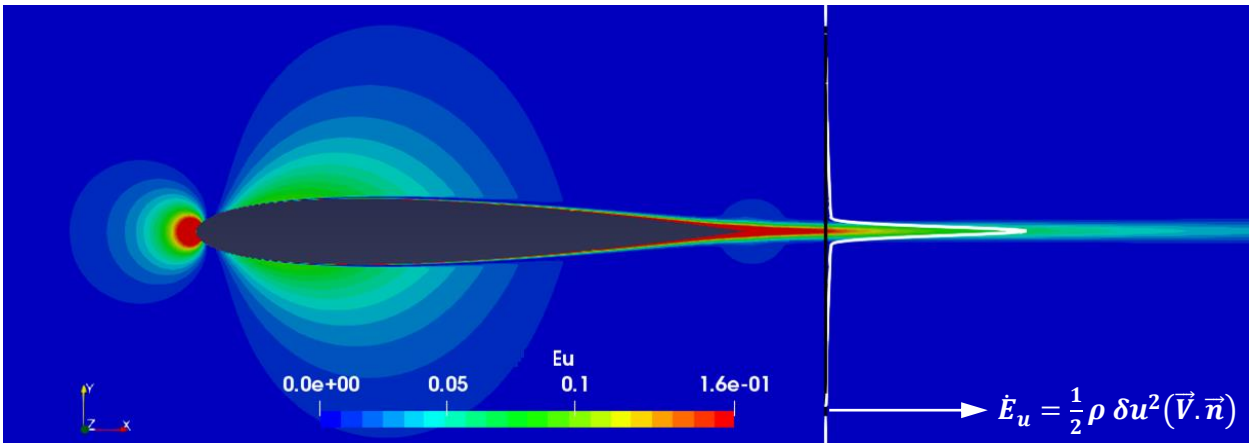

Fig. 6 Axial kinetic exergy field [adimensionalized]

This field is based on the square of the axial velocity perturbation field, thus the axial kinetic energy perturbation (i.e., the axial kinetic exergy) is positive throughout the domain independently of the sign of the velocity perturbation. This is because the exergetic approach considers that any velocity perturbation has a potential work to be recovered: it does not matter if the perturbation is an increase or a reduction of the speed, what matters is the perturbation itself. Note that there is a high work recovery potential at the leading edge, at the maximum airfoil thickness region and inside the wake/boundary layer. The work potential at the stagnation region and around the maximum thickness region of the airfoil is self-recovered as it will be seen later (it is not wasted). In fact, this is used by the velocity-pressure coupling mechanism of the isentropic flow. However, the axial kinetic exergy inside the wake is not recovered by the system: the airfoil uses its energy to create such perturbations whose work potential will be gradually destroyed along the wake by dissipation (anergy creation). Thus, all the wake's axial kinetic exergy that leaves a survey plane placed at the trailing edge represents a waste of exergy, but it also represents a room for improvements: this is the case of BLI configurations which re-energize the flow at this region by using a fan in order to reduce the velocity deficit downstream of the airframe, thereby reducing the axial kinetic exergy waste. Here it is reminded that the axial kinetic exergy leaving the trailing edge's survey plane outside of the wake is not a waste of exergy: this is still part of the isentropic pressure-velocity coupling so that the net total exergy related to the isentropic effect is zero (outside the wake) as it will be shown later.

By following the same systematic approach, it can be easily interpreted the transverse kinetic exergy field shown in Fig. 7, where its distribution along the black survey line is also shown.

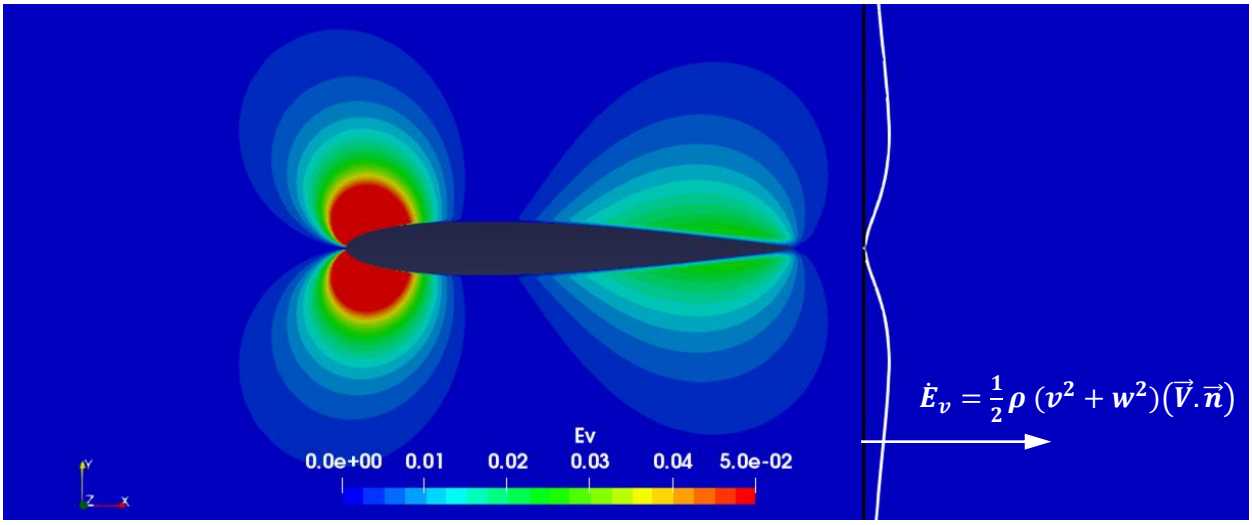

Fig. 7 Transverse kinetic exergy field

Again, the zones of high transverse exergy around the airfoil in the inviscid zone profit from the pressure-velocity mechanism, so it is not a wasted work potential. In addition, the transverse exergy leaving the survey plane outside of the wake also belongs to the isentropic velocity-pressure coupling so it is also not wasted even though it is convected downstream. However, it is interesting to note that the wake's transverse exergy is negligible for this flow condition.

The third component of the total mechanical exergy is the boundary-pressure work rate, whose field can be observed in Fig. 8. Note that any pressure perturbation around the airfoil inside the inviscid zone gives a negative value of the E_p parameter. This happens for example in the stagnation region at the leading edge, where the local static pressure is higher that the freestream static pressure, and at the same time, the local velocity is lower that the freestream velocity. On the other hand, at the top and bottom of the airfoil the behavior is the opposite: lower static pressure and higher velocity than freestream conditions. In all cases this leads to a local negative E_p value according to the Arntz formulation. Inside the boundary layer the situation is more complex. As a matter of fact, the local velocity is lower than the freestream velocity in the majority of its volume, so the velocity term is always negative. Thus, the sign of E_p will be driven by the local pressure: if the local pressure is lower than the freestream static pressure, then E_p will be positive and vice versa. The E_p parameter represents the work made locally on the fluid by the pressure difference respect to the equilibrium ambient pressure. Note that this work will occur only when a local velocity perturbation is present. Also note that its negative sign in the inviscid region means that not all the kinetic

exergy potential work shown before (Fig. 6 and Fig. 7) is completely available. In fact, part of the kinetic exergy potential work has been obtained at the expense of the pressure work.

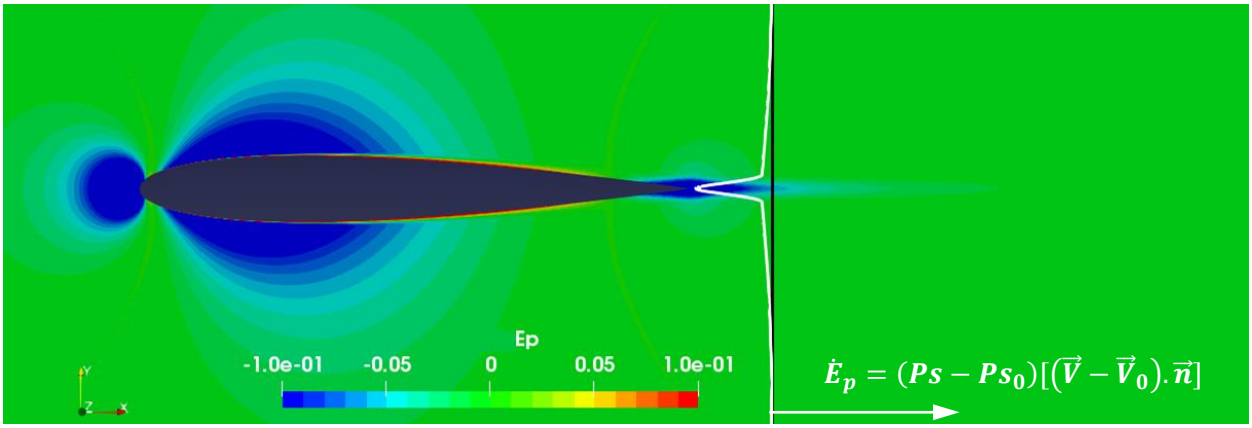

Fig. 8 Boundary-pressure work rate field

The addition of the 3 previously discussed fields gives the total mechanical exergy field as shown in Fig. 9. What must be noticed from this field visualization is that the local velocity perturbations are coupled with the local static pressure perturbations: as the flow is isenthalpic in the inviscid region, any kinetic energy perturbation must be paid by the local internal energy. This can be seen better in Fig.10, where the mechanical exergy is shown along a streamline lying outside the boundary layer (i.e., a streamline on the inviscid zone).

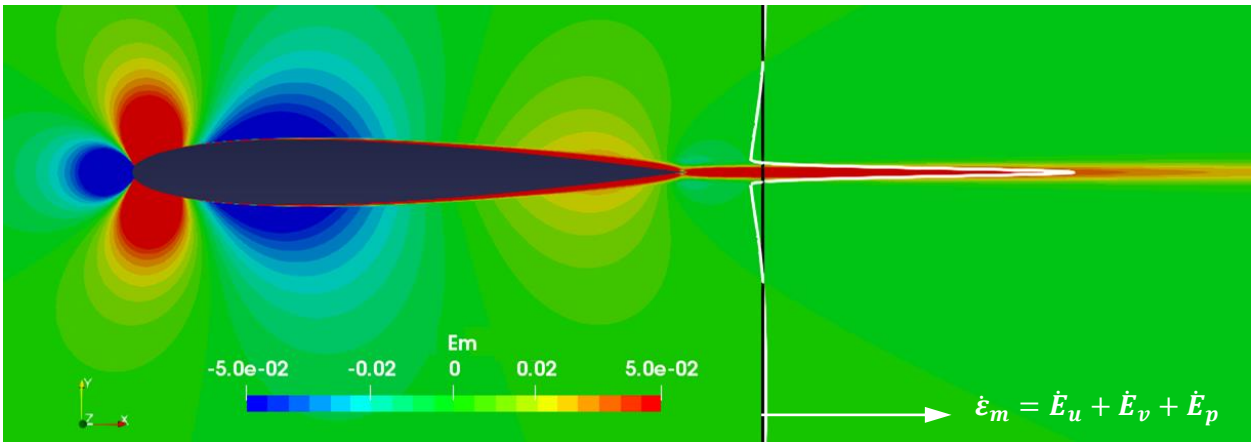

Fig. 9 Mechanical exergy field

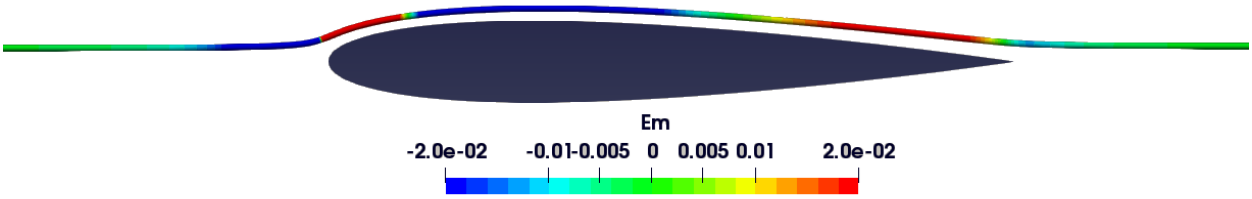

Fig. 10 Mechanical exergy along a streamline

A particle far upstream has zero mechanical exergy. So, theoretically, there is no current impetus to do further work. However it must perform some work in order to go around the airfoil. This is managed by using its own internal energy: firstly it accumulates pressure work in the stagnation region at the leading edge. Then it uses this work potential to vertically accelerate (gaining kinetic exergy) in order to go around the leading edge region. Then it cumulates work potential again in the high speed region in order to perform a vertical downwards acceleration on the rear part of the airfoil. Finally it accumulates pressure work again at the trailing edge in order to realign flow in the axial direction, reaching a final state with zero mechanical exergy. That's why the mechanical exergy in the inviscid zone is not an interesting parameter for design purposes (at least in 2D cases): its net mechanical exergy is zero, thus, there is no waste of exergy.

However the mechanical exergy inside the boundary layer and wake plays a major role on aircraft design as it is the potential advantage for BLI designs. A detail of the distributions of the mechanical exergy and its main components along the black survey line are shown in Fig. 11. This clearly depicts what was mentioned earlier: the axial kinetic exergy available inside the wake is not completely recoverable because it was obtained by doing some pressure work. The resulting net available exergy is the mechanical exergy inside the wake. This is the net exergy that will be gradually destroyed downstream by turbulent and viscous dissipation inside the wake (anergy generation). It also represents the maximum amount of energy that can be recovered by BLI systems.

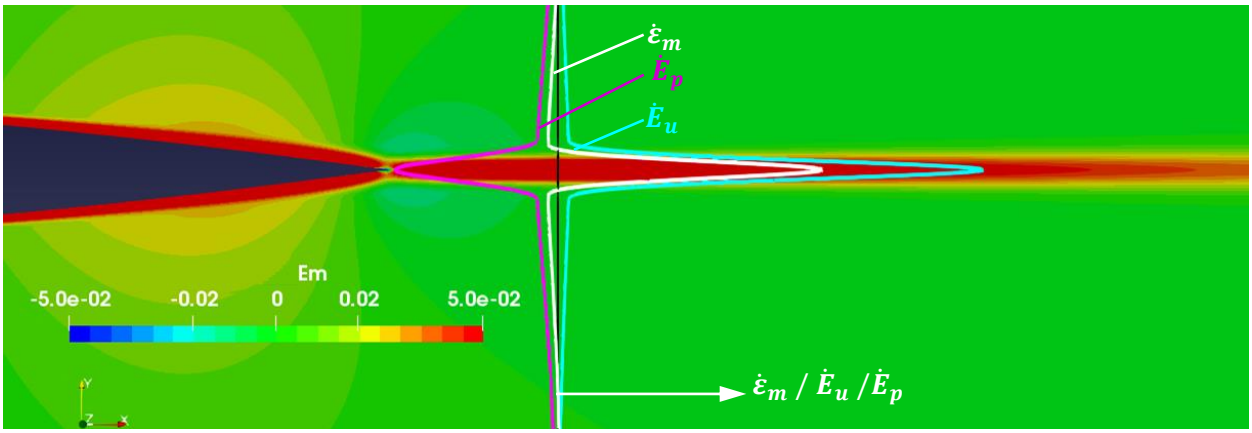

Fig. 11 "$\dot{E}_u$", "$\dot{E}_p$" and "$\dot{\varepsilon}_m$" distributions along the survey line

Up to this point we discussed the mechanical exergy. The thermal exergy will not be discussed here because it is negligible for unpowered vehicles without heat transfer.

The total anergy field and its distribution along a survey line are shown in Fig. 12. This represents the total loss of work potential that can be measured at each point of the domain. It takes into account the losses locally created at some point as well as the losses already created upstream and convected to this point. Note that there are no losses in the inviscid region as expected. All the losses come from the viscous regions (boundary layer and wake), where viscous, turbulent and thermal mixing effects take place (irreversible processes). This parameter is of main importance for designers who will be interested in reducing it, for example, by using laminar airfoils.

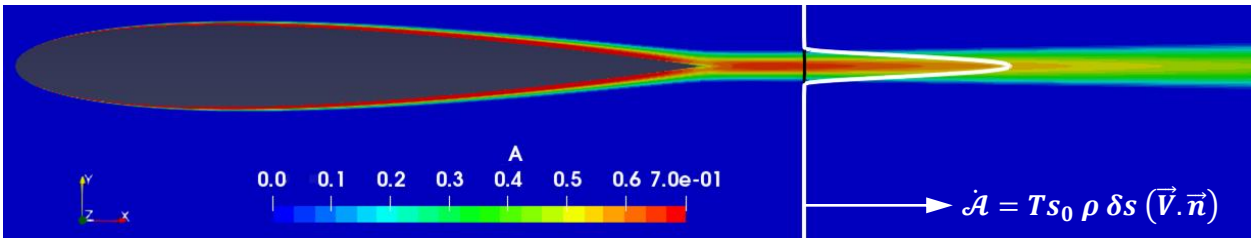

Fig. 12 Total anergy field

In order to detect the local spots where anergy is being created, it is more useful to visualize the viscous anergy and thermal anergy fields. This is because their formulations are based on a volume integral, thus their integrands represents the local creation of anergy. The total anergy discussed before is based on a surface integral formulation, thus its integrand already contains the upstream losses. The viscous anergy field is shown in Figure 13 where it can be observed that viscous losses occur inside the boundary layer and the wake. Also, a non-physical source of anergy is visible: this is the so-called "spurious anergy" and it is related to a strong numerical diffusion (this region lying

outside the boundary layer and wake must be deleted from the volume integral). Also note that viscous anergy is created in highly strained regions. This can be seen by the aid of the vorticity magnitude distribution along the survey line: it is clear that the viscous anergy is stronger at high-vorticity zones. This is because the viscous anergy is the work potential lost by viscous and turbulent dissipation.

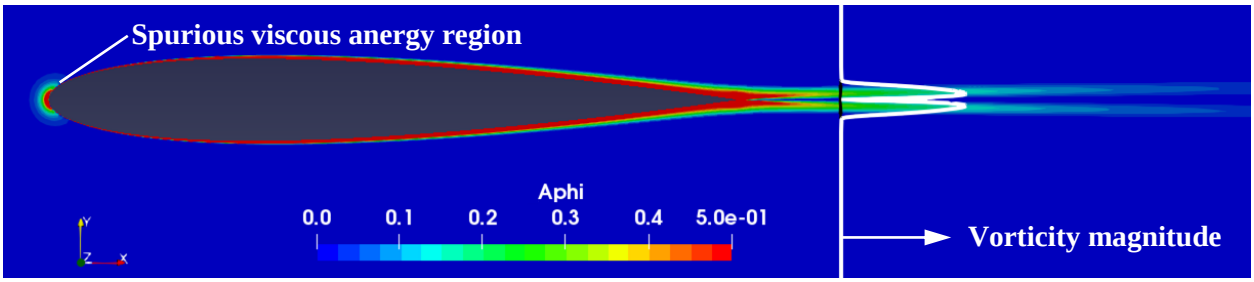

Fig. 13 Viscous anergy field

The thermal anergy field can be seen in Fig. 14. It represents the work potential loss by thermal mixing tending to homogenize any temperature field gradient (which has an inherent potential of doing some work). This explains why the thermal anergy is stronger inside the thermal boundary layer.

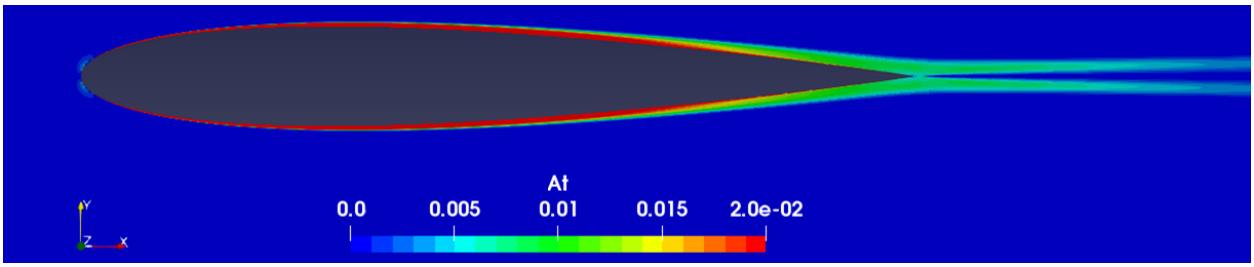

Fig. 14 Thermal anergy field

The study already presented shows the interest of using the exergy parameters for flow analysis because it provides an alternative point of view of the physics: the origin, nature, and intensity of losses are clearly visible with this method. In typical engineering applications, the sources of losses are usually visualized by the total pressure ratio (Fig. 15) or the entropy (Fig.16) fields (this later is mainly used by internal aerodynamicists). Nevertheless, these classical loss indicators give just a measure of the losses but they are not practical parameters: it is not easy for an engineer to relate those fields directly with the drag, mainly because of the units inconsistency between them. The advantage of the exergetic approach is that it gives the losses in a far more tangible unit: Watts (when it is integrated along the survey line or the integration volume) or Watts per unit of volume/surface (when its integrand is visualized on the field). This allows the design engineer to be aware of the power consumed or wasted locally by an

aircraft, and ultimately to know the amount of power (exergy) to be supplied by the engine in order to reach the flight equilibrium. This high-level vision of the aerodynamic assessment makes the Exergy Method a good candidate for the physical analysis, and consequently for a system-level aircraft design.

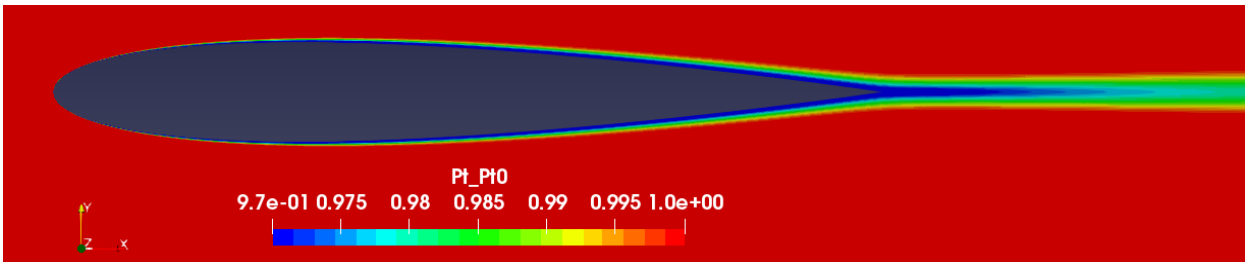

Fig. 15 Total pressure ratio (Pt/Pt0)

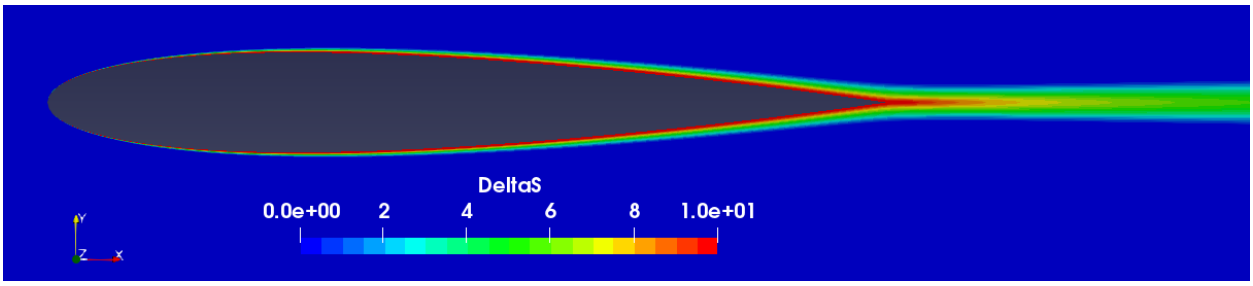

Fig. 16 Entropy variation field [J/kg K]

Another meaningful way to analyze losses used routinely for design purposes is the drag density field visualization shown in Fig. 17. Here, the integrand of the Meheut's equation is plotted at every point of the domain (that's why it is called "density field"). The integral of this density along the survey line gives the total profile drag in Newtons, thus, it is preferable to use this parameter rather than the total pressure ratio or the entropy fields. However, the disadvantage of this approach compared to the Exergy Method is that the far-field method does not allows detecting the different sources of losses (i.e., to perform a flow field breakdown for 2D subsonic cases). On the other hand, note that both methods are equivalent because they are different formulations describing the same physics. Thus, if drag losses are only measurable inside the wake and not on the inviscid region as shown in Fig. 17, the same must be also valid for the exergy approach. This confirms the statement made before: the mechanical exergy outside the wake (i.e., lying on the inviscid region) must not be considered as a loss and it does not have any engineering interest for design purposes. Only the mechanical exergy available inside the wake represents a waste of work potential.

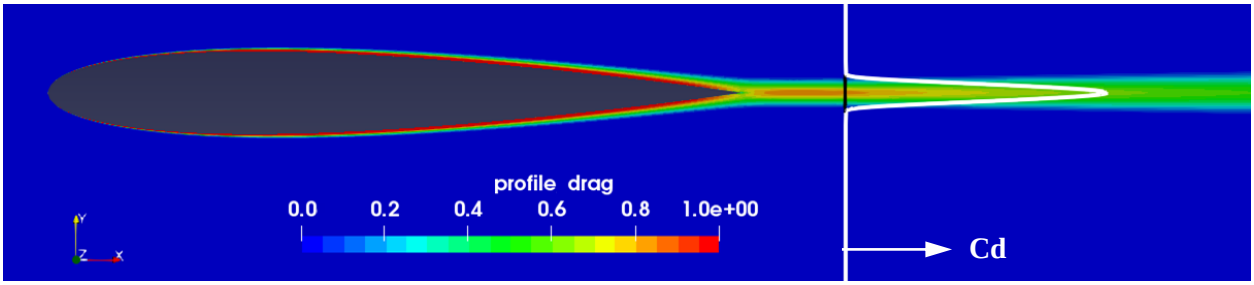

Fig. 17 Profile drag density field

Here it is interesting to compare the drag distribution for the two methods: Meheut and Arntz. In order to do so, a survey line is placed downstream far enough in order to avoid the potential effect on the exergetic method as shown in Fig. 18 (where the survey plane is placed at 1.5 chords downstream of the trailing edge of the airfoil). At that position, the profile drag density distribution for the Meheut and Exergy methods are displayed (white and red curves respectively). Their integrals gives the same drag coefficient, however, their distributions are not identical: the Meheut method overestimates the profile drag density at the center of the wake, while it underestimates this value at the outer part of the wake (taking the exergy distribution as a reference, because it is based on exact equations while the Meheut method is based on a small perturbations approximation).

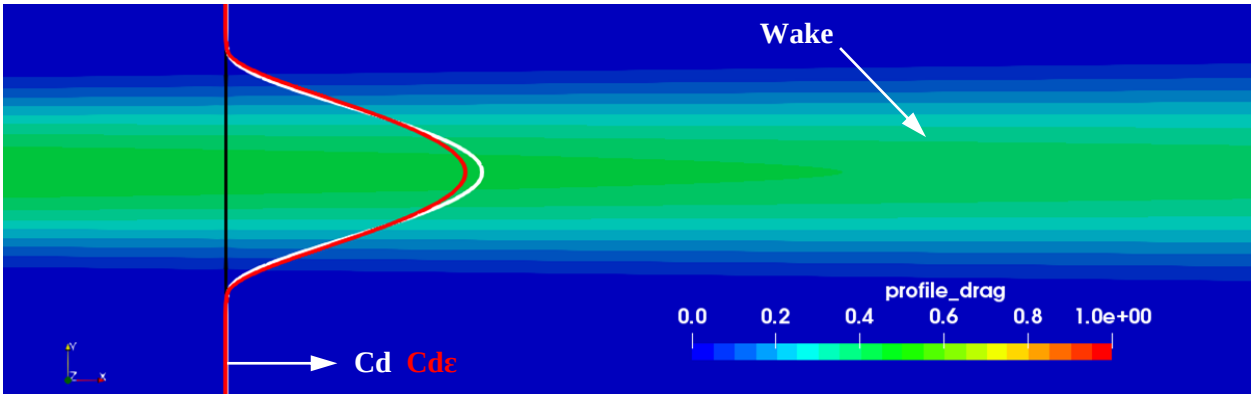

Fig. 18 Profile drag density and exergy-based drag density distributions along the survey line

B. M=0.3 / α=10°

The following analysis studies a more complex condition: the airfoil at high angle of attack. Its axial kinetic exergy field is shown in Fig. 19, including its distribution along a survey line normal to the infinite upstream flow direction. It is clear that there is a high axial kinetic exergy spot at the stagnation region as well as at the upper surface region. This last one is the most exergetic because of the high speed perturbation related to the circulation

(lift). On the other hand, the flow has not been accelerated around the lower surface, which explains the low level of axial kinetic exergy in this region. Also note the large amount of axial kinetic exergy available inside the wake.

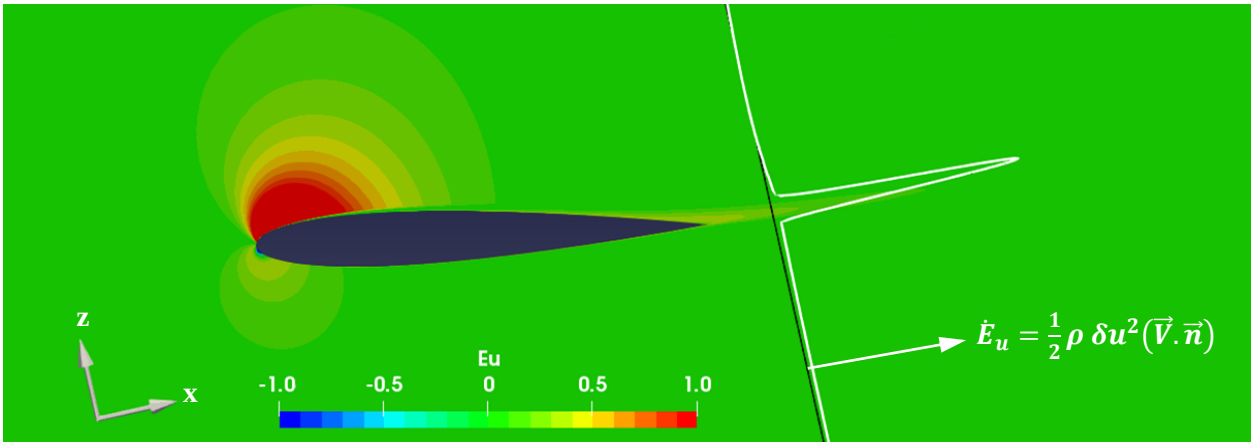

Fig. 19 Axial kinetic exergy field

For high angles of attack the axial kinetic exergy is not positive in the entire flow field (as it was shown for the zero angle of attack case in Fig. 6). This can be better observed in Fig. 20, where a detail of the leading edge flow pattern is shown. Note that the flow has a negative x-velocity component locally at the left of the stagnation point, which gives place to a negative flux of the "δu^2" term, leading to a negative value of "$\dot{E}_u$". However, this negative sign does not call into question the fact that there is an axial kinetic exergy available there.

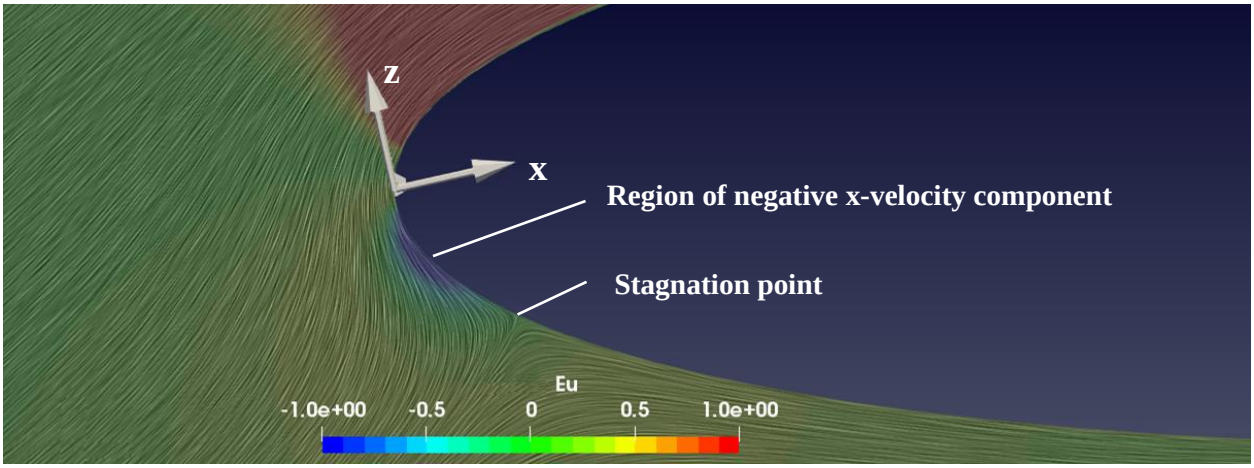

Fig. 20 Detail of the axial kinetic exergy field at the leading edge

Fig. 21 presents the transverse kinetic exergy field as well as its distribution along a survey line. Again an upwards kinetic energy region is found around the upper surface at the leading edge and a downwards kinetic energy region towards the trailing edge at the upper surface. Nevertheless, the vertical velocity components around the lower surface are very small, leading to an insignificant amount of transverse kinetic exergy on that region.

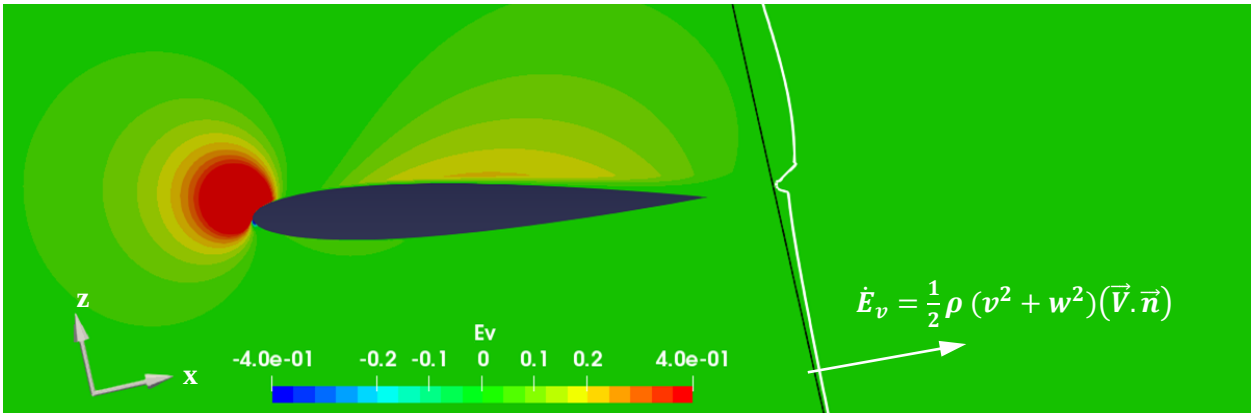

Fig. 21 Transverse kinetic exergy field

Fig. 22 shows the boundary-pressure work rate field and its distribution along a survey line. Note that the stagnation point is placed under the leading edge, leading to a high negative pressure work in that region. Besides, the negative boundary-pressure region around the upper surface has been expanded and intensified respect to the zero angle of attack case, but the one at the lower surface have almost disappeared. Moreover, the wake still contains some negative boundary-pressure work rate as discussed before.

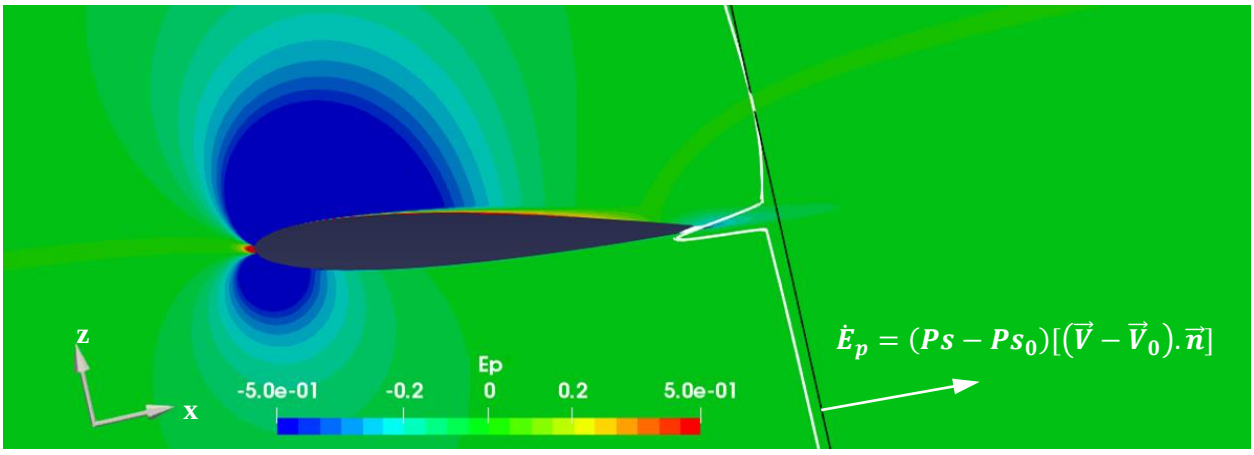

Fig. 22 Boundary-pressure work rate field

The resulting total mechanical exergy field is shown in Fig. 23. It can be seen that the boundary layer related exergy has been increased respect to the zero incidence case in the upper surface region (because of the boundary layer thickening), but reduced on the lower surface. The net resulting wake exergy outflow remains similar to the zero angle of attack case. On the other hand, the inviscid region continues to behave as expected for an isenthalpic flow as shown in Fig. 24, where the exchanges of pressure work and kinetic exergy are depicted for a streamline lying outside the boundary layer as it was explained before.

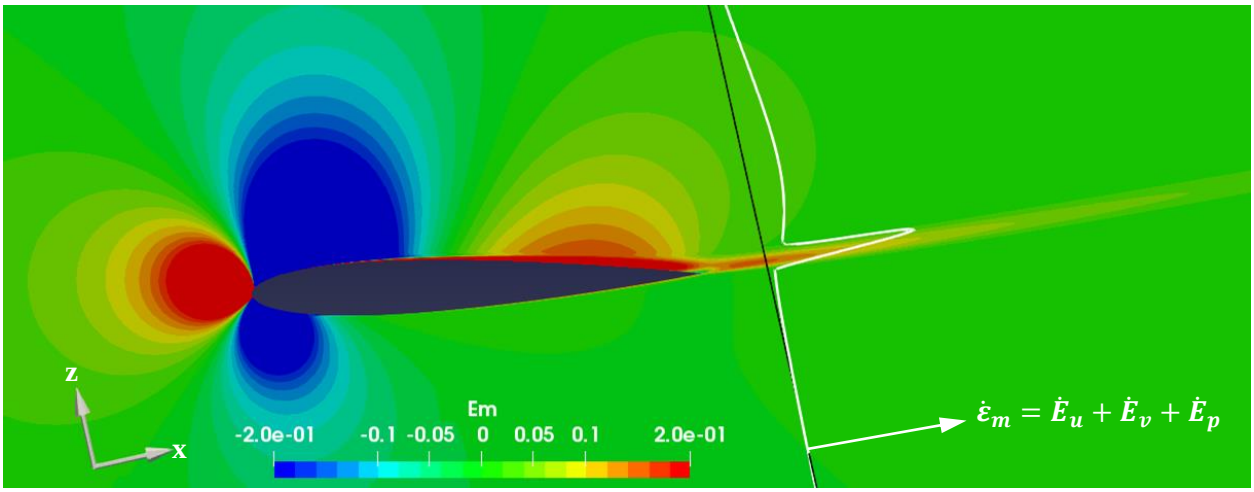

Fig. 23 Mechanical exergy field

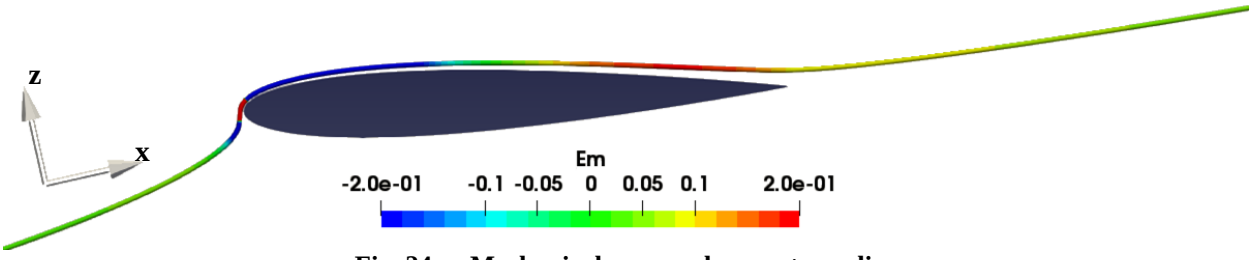

Fig. 24 Mechanical exergy along a streamline

The total anergy field and its distribution along the survey line are shown in Fig. 25. It shows the boundary layer thickening at the upper surface and its strong shear inside the boundary layer; this leads to higher losses than the zero angle of attack case which explains the increase of the profile drag with the angle of attack. Moreover, these losses are convected downstream but the turbulent mixing tends to homogenize its distribution.

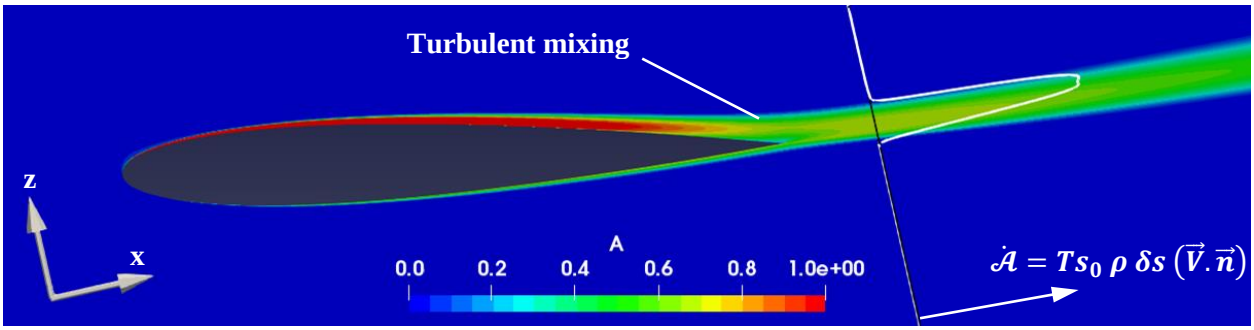

Fig. 25 Total anergy field

Figure 26 displays the spots where viscous anergy is being created by viscous dissipation and turbulence, and Fig. 27 shows the thermal mixing losses. Note that the boundary layer losses are concentrated towards the first part of the airfoil because the local strain is stronger there. Also note that the boundary layer volume and the related

losses are larger than the zero angle of attack case. This explains why the anergy increases with the angle of attack [16]. Here it is reminded that the spurious anergy zone around the leading edge (outside the boundary layer) must not be taken into account for the analysis.

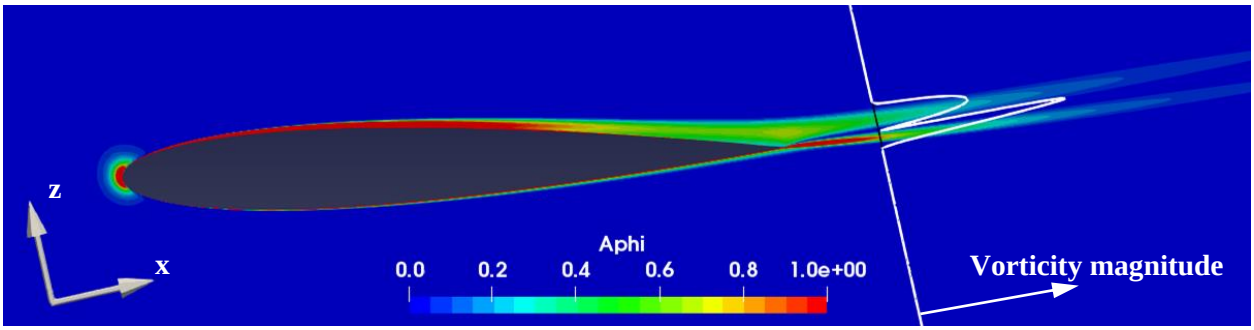

Fig. 26 Viscous anergy field

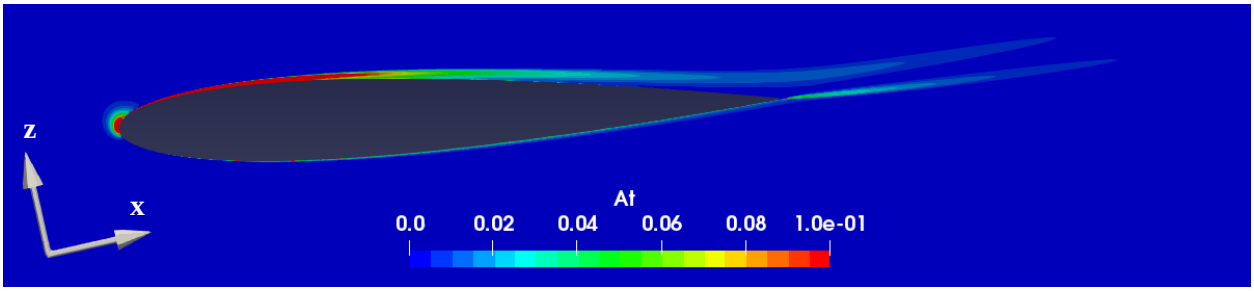

Fig. 27 Thermal anergy field

The profile drag density field for the Meheut method is shown in Fig. 28. Again, this method only displays the profile drag density but it does not enables a drag breakdown for 2D subsonic cases. This breakdown is feasible with the exergy method, which shows its advantage for the analysis of flows.

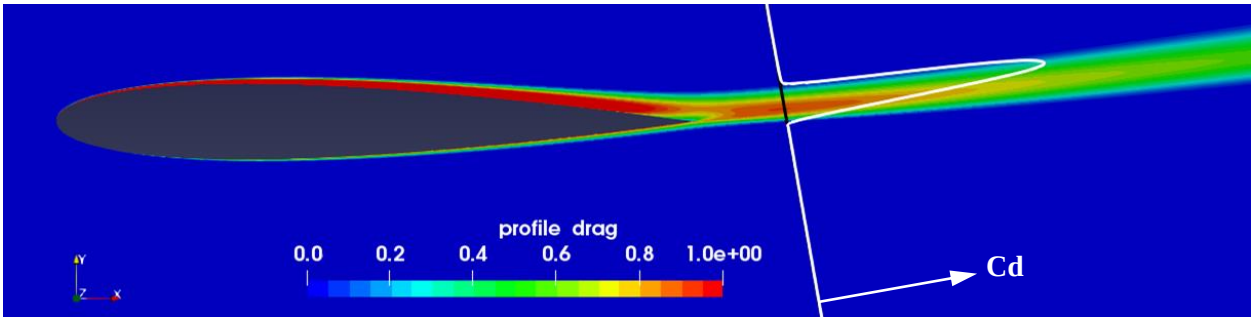

Fig. 28 Profile drag density field

C. M=0.8 / α=0°

In order to analyze the changes in transonic conditions, the same airfoil is studied at Mach number of 0.8 with zero angle of attack. Its related axial kinetic exergy field is observed in Fig. 29 where a high axial kinetic exergy

region is present in the supersonic zone, followed by a zone of little kinetic exergy downstream of the shockwave. Indeed, the axial velocity reduction across the shockwave is at the origin of this sudden loss of kinetic energy. Again, the only interesting exergy from the design point of view is the kinetic exergy contained inside the non-isentropic regions, i.e., the viscous region (boundary layer and viscous wake) as well as the shockwave wake region.

The transverse kinetic exergy field can be observed in Fig. 30. It does not show major changes compared to the subsonic case with zero angle of attack because the supersonic region and its related shockwave affects mainly the x-velocity component.

The boundary-pressure work rate field is observed in Fig. 31, where the supersonic region presents a huge accumulation of work.

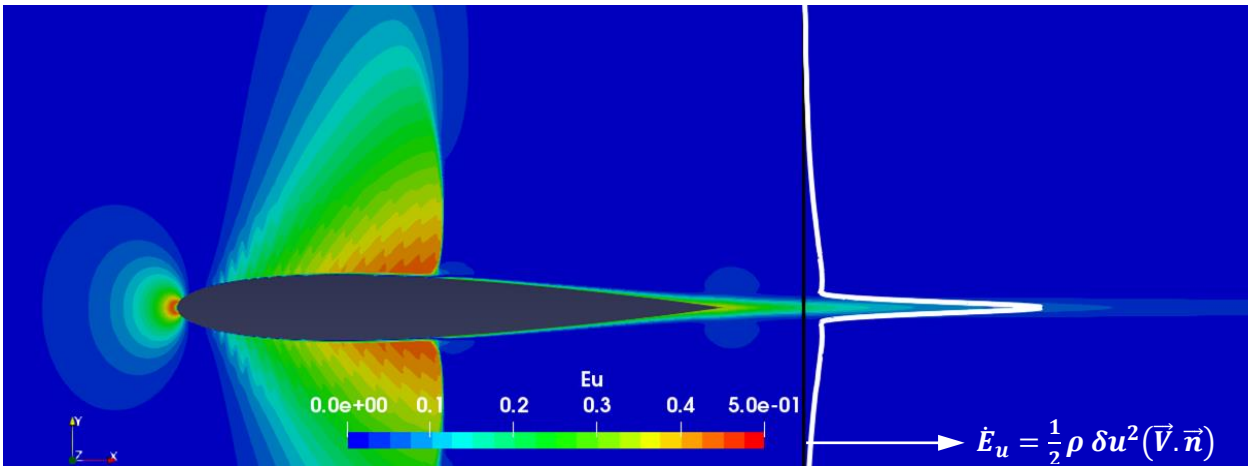

Fig. 29 Axial kinetic exergy field

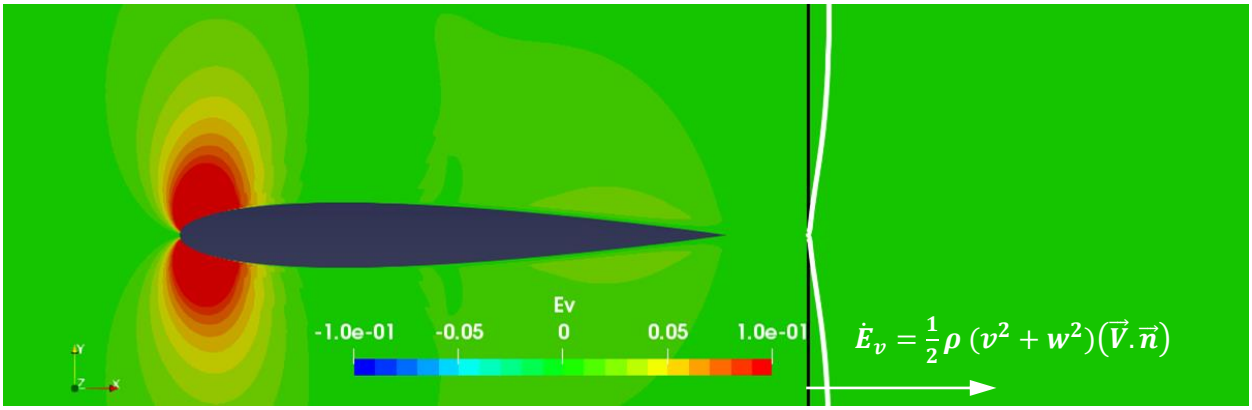

Fig. 30 Transverse kinetic exergy field

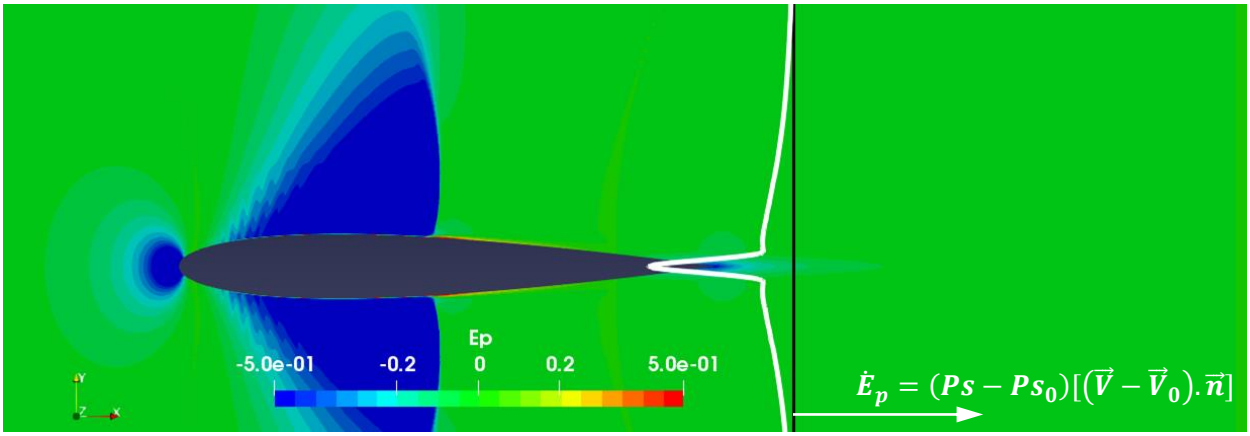

Fig. 31 Boundary-pressure work rate field

The final mechanical exergy field, given by the addition of the 3 previous fields, is shown in Fig. 32. The distribution of this field along a survey line placed very close to the body is also shown in this figure. However, for this position of the survey line, the potential effect of the body masks the fact that a net mechanical exergy is also available on the shockwave wake. Indeed, if the survey line is placed farther as shown in Fig. 33, the mechanical exergy profile clearly shows a net exergy available in the shockwave wake region (green zone), placed around the viscous wave (red zone). This means that the shockwave wake also offers a room for design improvement, by performing a shockwave wake ingestion (SWI), equivalent to the BLI.

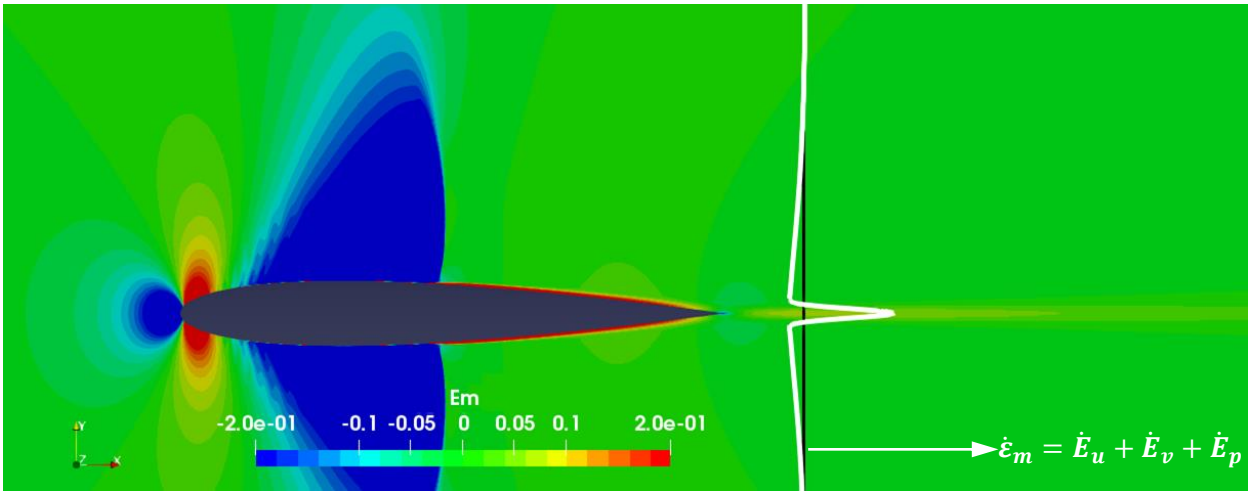

Fig. 32 Mechanical exergy field

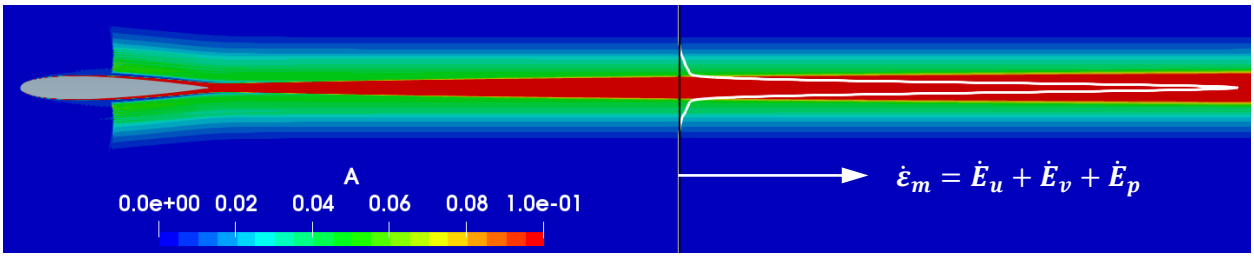

Fig. 33 Mechanical exergy along a survey plane placed at x/C=2.5

The total anergy field is shown in Fig. 34 where it can be seen that losses are created across the shockwave because of its non-isentropic process; these losses are then convected downstream along its wake. The intensity of the shockwave losses is smaller than the viscous losses, but it occupies a larger region, thus the total wave anergy is comparable in magnitude to the viscous/thermal anergies inside the boundary layer. This can be better seen by the total anergy distribution along the survey line.

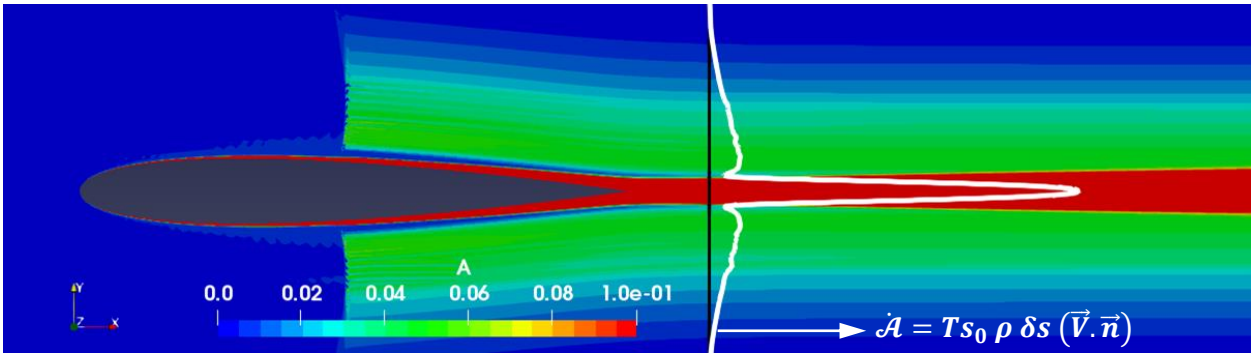

Fig. 34 Total anergy field

The other way to observe the sources of the losses is by analyzing the volume formulation of the total anergy components. The viscous anergy field in Fig. 35 shows the same pattern observed on the subsonic case but this time the shockwave viscous losses are also visible.

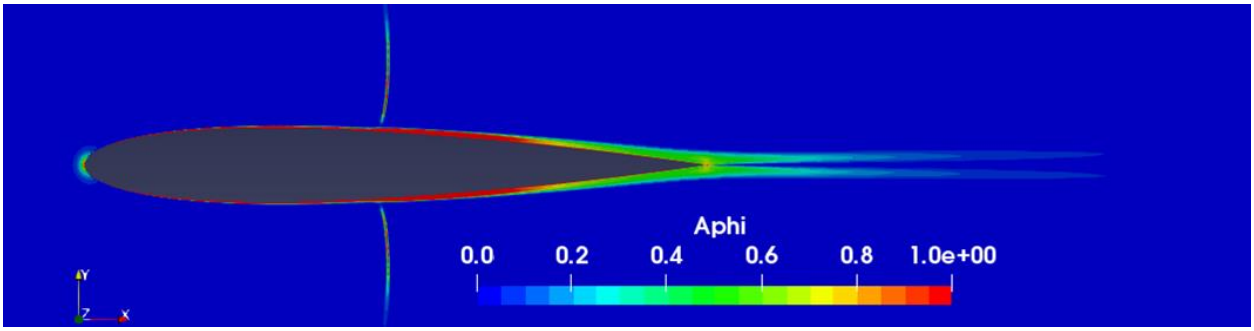

Fig. 35 Viscous anergy field

The same observations are valid for the thermal anergy field in Fig. 36 and the wave anergy field in Fig. 37. However, in this last case care must be taken because the divergence formulation is used to visualize the entire flow field; however, the region to be integrated (and the only one having a physical meaning) is the volume around the shockwave, as it is highlighted in Fig. 37.

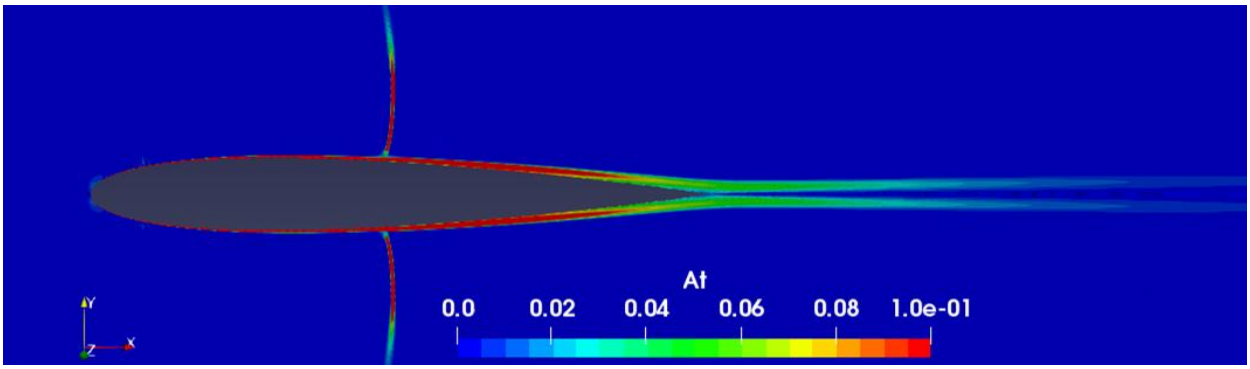

Fig. 36 Thermal anergy field

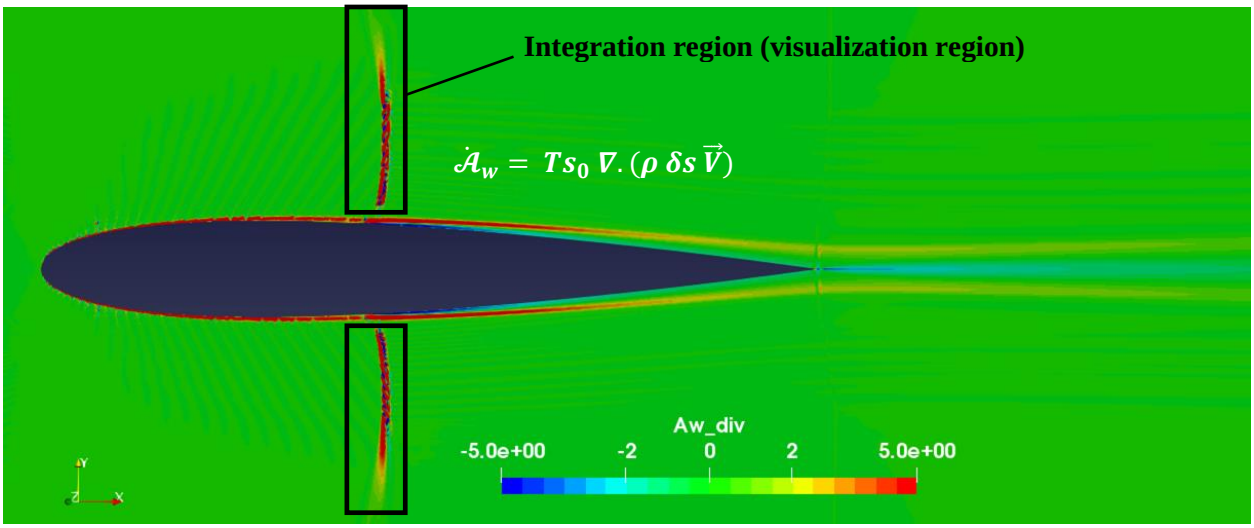

Fig. 37 Wave anergy field (by divergence approach)

One of the advantages of the surface integral formulations (as it was the case of the total anergy) is that it displays the accumulation of the losses along a streamline up to the survey plane position. On the other hand, the volume formulations (e.g., viscous anergy) identify the spots of losses and their intensity, but they do not take into account the convection downstream. The combined use of both approaches is very useful in order to understand the flow field losses.

Finally, the profile drag density field by Meheut's method is shown in Fig. 38. A comparison of both methods is shown in Fig. 39, where the exergy-based drag is shown in white line and the momentum-based drag profile is shown in blue.

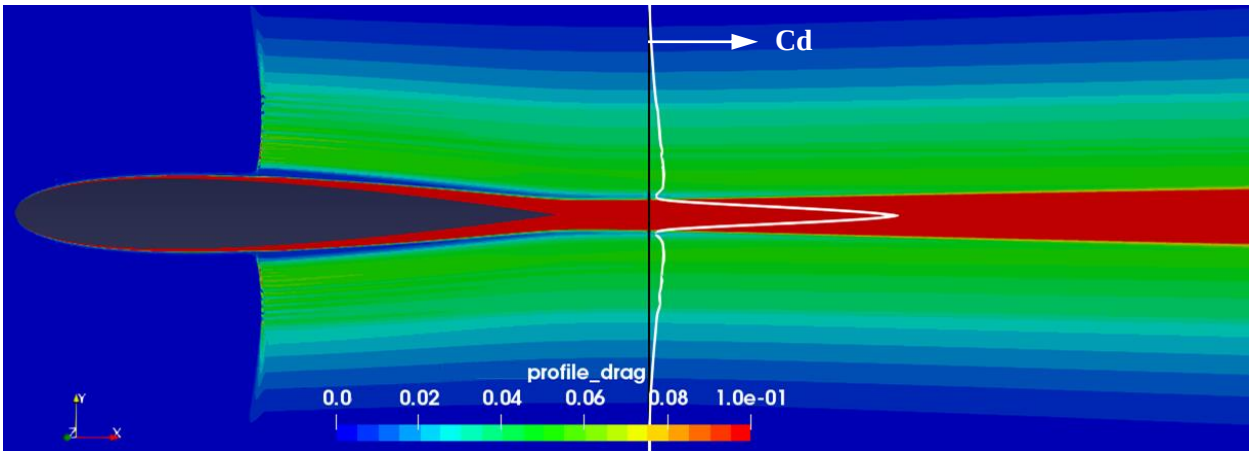

Fig. 38 Profile drag density field

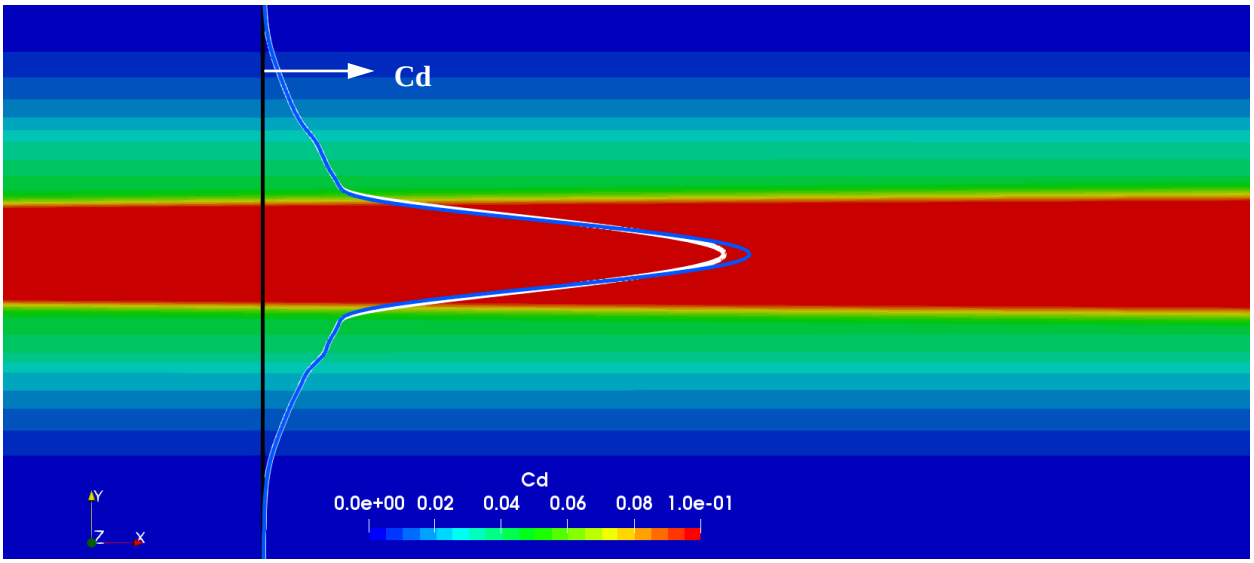

Fig. 39 Profile drag density and exergy-based drag density distributions along the survey line

It can be seen that the same physical phenomena is captured by both methods. Moreover, for transonic cases the far-field method performs a drag breakdown of the profile drag into the wave and viscous drag by using the Kusunose technique [16, 20], but this is not as complete as the exergetic-based drag breakdown.

V. Conclusion

This work has shown the strong potential of the exergetic method to perform a flow field analysis of classical configurations like an airfoil. This is because the exergy method offers a powerful insight into the physics thanks to

its intuitive and easy to understand formulation. The visualization of the exergy parameters enabled a deep aerodynamic assessment of the losses origin. These losses ultimately become the profile drag coefficient. It was demonstrated that the surface integral anergy formulation shows the convected losses and the volume integral formulations shows the actual spots where anergy is being created. This is very useful for aircraft design purposes because it enables the identification of the zones where the engineer must pay attention in order to improve the design. On the other hand, the interpretation of the mechanical exergy field was presented and its importance for design purposes was highlighted. Moreover, it was demonstrated that the exergy method allows performing a more complete drag breakdown on the entire flow field (compared to the far-field method), enabling deepest flow field analyses. Thus, this approach can be used to complement the classical flow field analysis methods in order to reach a very high physical understanding.

VI. References

[1] Meheut, M., "Evaluation des Composantes Phénoménologiques de la Trainée d'un Avion à Partir des Résultats Expérimentaux," Thèse ONERA-Université des Sciences et technologies de Lille, France, 2006.

[2] Drela, M., "Power Balance in Aerodynamic Flows," *AIAA journal*, Vol. 47, No. 7, 2009, pp. 1761-1771. DOI: 10.2514/1.42409

[3] Arntz, A., "Civil Aircraft Aero-thermo-propulsive Performance Assessment by an Exergy Analysis of High-fidelity CFD-RANS Flow Solutions," Fluids mechanics, Université de Lille 1, 2014.

[4] Hall, D., "Boundary Layer Ingestion Propulsion: Benefit, Challenges and Opportunities," 5th UTIAS International Workshop on Aviation and Climate Change, Toronto, Canada, 20th may 2016.

[5] Tailliez, C., Arntz, A., "CFD Assessment of the Use of Exergy Analysis for Losses Identification in Turbomachine Flows," 53rd 3AF International Conference on Applied Aerodynamics, 26 – 28 March 2018, Salon de Provence, France

[6] Betz, A., "A Method For The Direct Determination of Wing-Section Drag," NACA Technical Report 337, 1925.

[7] Jones, B., "Measurement of Profile Drag by the Pitot-Traverse Method," Aeronautical Research Council R&M Rept. 1688, 1936.

[8] Oswatitsch, K., *Gas Dynamics*, Academic Press, New York, 1956.

[9] Kusunose, A., "Extension of Wake-Survey Analysis Method to Cover Compressible Flows," *Journal Of Aircraft*, Vol. 39, No. 6, 2002, pp. 954-963.

[10] Cengel, Y., Boles, M., *Thermodynamics: An Engineering Approach*, Mc Graw Hill Education, New York, 2015.

[11] A.Bejan, *Advanced engineering Thermodynamics*, Second edition, John Wiley and Sons, New York, 1997.

[12] D. Riggins, Moorhouse, D., Camberos, J., "Characterization of Aerospace Vehicle Performance and Mission Analysis Using Thermodynamic Availability," *Journal of Aircraft*, Vol. 47, No. 3, 2010, pp. 904-9016.

[13] Li, H., Stewart, J., Figliola, R., "Exergy Based Design Methodology For Airfoil Shape Optimization And Wing Analysis," 25th International Congress Of The Aeronautical Sciences ICAS, 3rd – 8th September, Germany, 2006.

[14] Alabi, K., Ladeinde, F., Spakovsky, M., Moorhouse, D. and Camberos, J., "The Use Of The 2nd Law As A Potential Design Tool For Aircraft Air Frame Subsystems," *International Journal of Thermodynamics*, Vol. 9 (No. 4), 2006, pp. 193-205. ISSN 13019724.

[15] Camberos, J. and Moorhouse, D., *Exergy Analysis and Design Optimization for Aerospace Vehicles and Systems*, Progress in Astronautics and Aeronautics, AIAA, 2011. eISBN: 978-1-60086-840-5

[16] Aguirre, M. and Duplaa, S., "Exergetic Drag Characteristic Curves," *AIAA Journal*, accepted for publication in March 2019.

[17] McCroskey, W., A Critical Assessment of Wind Tunnel Results for the NACA 0012 Airfoil, NACA TM 100019, 1987.

[18] Ladson, C., Effect of Independent variation of Mach and Reynolds numbers on the Low-Speed aerodynamic Characteristics of the NACA 0012 airfoil section, NACA TM 4074, 1988.

[19] AGARD, "Experimental Data Base For Computer Program Assessment," *AGARD Advisory Report No. 138*, 1979.

[20] Kusunose. A, Crowder, J., Watzlavick, Z., "Wave Drag Extraction from Profile Drag Based on a Wake-Integral Method," AIAA 99-0275, 37th AIAA Aerospace Sciences Meeting and Exhibit, January II-14, 1999. https://doi.org/10.2514/6.1999-275